INTERNATIONAL JOURNAL FOR NUMERICAL AND ANALYTICAL METHODS IN GEOMECHANICS
Int. J. Numer. Anal. Meth. Geomech. 2009; **33**:1535–1560
Published online 18 February 2009 in Wiley InterScience (www.interscience.wiley.com). DOI: 10.1002/nag.777

An extended finite element framework for slow-rate frictional faulting with bulk plasticity and variable friction

Fushen Liu and Ronaldo I. Borja*, †

Department of Civil and Environmental Engineering, Stanford University, Stanford, CA 94305, U.S.A.

SUMMARY

We present an extended finite element (FE) approach for the simulation of slow-rate frictional faulting in geologic media incorporating bulk plasticity and variable friction. The method allows the fault to pass through the interior of FEs without remeshing. The extended FE algorithm for frictional faulting, advocated in two recent articles, emanates from a variational equation formulated in terms of the relative displacement on the fault. In the present paper we consider the combined effects of bulk plasticity and variable friction in a two-dimensional plane strain setting. Bulk plasticity is localized to the fault tip and could potentially be used as a predictor for the initiation and propagation of new faults. We utilize a variable velocity- and state-dependent friction, known as the Dieterich–Ruina or 'slowness' law, formulated in a slip-weakening format. The slip-weakening/variable friction model is then time-integrated according to the generalized trapezoidal rule. We present numerical examples demonstrating the convergence properties of a global Newton-based iterative scheme, as well as illustrate some interesting properties of the variable friction model. Copyright © 2009 John Wiley & Sons, Ltd.

Received 16 August 2008; Accepted 17 December 2008

KEY WORDS: extended finite element; friction; fault; plasticity

1. INTRODUCTION

Simulation of frictional faulting with the finite element (FE) method is one of the most challenging problems in computational mechanics. Faults are not simply frictional contacts of bare rock surfaces; they are usually lined with wear detritus, called cataclasite or fault gouge [1, 2]. The

*Correspondence to: Ronaldo I. Borja, Department of Civil and Environmental Engineering, Stanford University, Stanford, CA 94305, U.S.A.
†E-mail: borja@stanford.edu

Contract/grant sponsor: US Department of Energy; contract/grant number: DE-FG02-03ER15454
Contract/grant sponsor: National Science Foundation; contract/grant number: CMG-0417521
Contract/grant sponsor: Stanford Graduate Fellowship

analyst faces the uncertain direction of fault rupture and propagation in a structured FE grid, as well as the complicated processes associated with fault movement including degradation of the material properties within the fault zone and the thickening of the fault gouge [3]. Large-scale simulation of frictional faulting often inhibits an explicit treatment of smaller-scale processes leading to the next larger-scale processes, such as micro-cracking and coalescence of smaller-scale fractures and their upscaling to the fault scale. On the other hand, it is known that the effective friction coefficient on a fault depends on the extent of damage in the fault zone. For example, the coefficient of friction may be expected to be higher near the fracture process zone around the fault tip than in the fully developed sliding zone [4–7]. To circumvent these difficulties, it is usually prudent to select a reference scale for analysis (fault scale in the present work) and either downscale or upscale the other processes to bring all processes to a common scale in a meaningful way.

In this work we select the fault scale (typically on the order of kilometers in our numerical examples, the dimensions are all on the order of meters) for reference and develop an FE framework for capturing important processes of fault rupture and propagation. A first challenge concerns the uncertain direction of fault propagation against the backdrop of a fixed FE grid. Several FE enhancement techniques have been advanced in the literature (see Borja [8] for a brief survey) that capture the presence of a discontinuity in a fixed FE grid. In this paper we use the extended FE technique [9–17]. This technique embeds a strong discontinuity into a fixed FE mesh through the introduction of additional degrees of freedom to existing nodes, which are then determined along with the regular nodal degrees of freedom in one combined global equation solve. Unlike the classical strong discontinuity approach where slip is interpolated using a piecewise constant function [18–27], the extended FE technique permits a higher-order interpolation of slip that is continuous across element boundaries.

Geologic faults evolve from shearing across a series of echelon joints forming pockets of highly damaged rock. As shearing progresses, a fault core, or cataclasite zone, develops between surrounding less damaged zones made up of joints and sheared joints. As one moves farther away from the fault core, the rock becomes less and less damaged, until one finds the competent 'host' rock that marks the end of the fault zone [3]. Most of the offset or slip between the surrounding rock occurs at the cataclasite zone where rocks could be reduced to a very fine-grained clay-like material due to all the slipping and grinding [28]. Because the fine-grained materials in the cataclasite zone may be considered frictional in nature, fault zones are also considered frictional. However, it must be noted that the effective friction coefficient on a fault is derived from upscaling the frictional properties of the fine-grained materials comprising the fault core. Therefore, the coefficient of friction of a fault is expected to vary with degree of damage on the host rock.

Extensive studies have been conducted to understand the frictional constitutive behavior of two contacting rock surfaces under slow-rate shearing. A widely accepted constitutive law that is currently in best agreement with experimental data [29] is the Dieterich–Ruina friction or 'slowness' law [30–32], where the coefficient of friction is shown to vary with slip speed as well as with a state variable reflecting the maturity of contact. Dieterich [33] later showed that this friction law is accurate not only for rocks but also for other materials such as glass and acrylic plastic. Tests conducted to validate this friction law involved shearing of two bare surfaces, so some adjustment might have to be made to extrapolate the results to prototype faulting scenarios as well as to faster loading conditions. However, this friction law has a logarithmic/exponential form that is complex enough to challenge the most robust nonlinear iterative solver. Selection of this power law does appear to be warranted for testing the robustness of the proposed extended FE formulation.

DOI: 10.1002/nag

During the initial stage of slip instability a fault zone experiences slip-weakening where the sliding strength on the fault decreases from a certain peak level to a certain residual value. For intact or relatively undamaged rocks, the peak resistance may consist of frictional and cohesive components along potential sliding surfaces, whereas for previously faulted rocks the peak resistance may consist primarily of frictional components. Borja and Foster [34] described the complex interplay between cohesive softening and friction hardening during the narrow time window of slip weakening in a general 3D state of stress. They also inferred the general 3D slip-weakening model to the experimental measurements and simplified (to certain stress configurations) models of [35–40]. Slip weakening introduces an additional nonlinearity to the governing field equations as it bridges two distinct deformation states in the faulting process. Furthermore, as the term 'weakening' suggests, the deformation process involves loss of strength, or softening, which could lead to numerical instability.

Bulk plasticity usually occurs around the fault tip where strain concentrates. No material can withstand an infinite stress, so yielding is expected where stress exceeds the yield value, and this usually occurs around the fault tip. Irwin [41, 42] argued that the occurrence of plasticity around the tip makes a crack behave as if it was longer than its actual size since plastic deformation causes the displacements to increase and the stiffness to decrease relative to the elastic case. Dugdale [43] and Barenblatt [44] employed similar approaches of considering an effective crack that is longer than the original physical crack to determine the extent of the yield zone, whereas Bilby *et al.* [45] later investigated the spread of plastic yield zone from a notch. Recent advances in computational plasticity, along with strong discontinuity kinematics, allow the detection of plastic deformation not only around the fault tip but also on the sliding part of the fault itself. Foster *et al*. [21] used strong discontinuity analysis based on the assumed enhanced strain formulation and attributed the occurrence of bulk plasticity on the sliding part of a fault to locking induced by the more constrained kinematics in a curved fault. Sanz *et al.* [46, 47] utilized large deformation contact mechanics to infer the occurrence of plasticity and strain localization around the fault tip underneath an asymmetric anticline as well as to regions much farther away in front of the fault tip.

A pressing challenge concerns the ability of an FE algorithm to handle extreme nonlinearities arising from combined effects of strong discontinuity enhancements, bulk plasticity, slip weakening, and variable friction. Foster *et al*. [21] show that an enhanced FE framework for strong discontinuity based on assumed enhanced strain can handle such combined nonlinearities in the simulation of prototype boundary-value problems. The present paper aims to build upon the results of this previous work and demonstrate that a framework based on the extended FE method can handle extreme nonlinearities just as well. We limit the scope of this paper, however, to deformation-controlled simulations in the presence of slip weakening. Arc-length type iterative algorithms [48] may be better suited for load-driven problems in the presence of softening, which is not covered in the present work.

2. MECHANICAL PROCESSES AND CONSTITUTIVE LAWS

Faulting involves highly complex mechanical processes including nucleation, weakening, slip propagation, and frictional sliding. The constitutive laws are equally complex, particularly those governing fault tip deformation and the variable friction law. This section outlines the mechanical processes and associated constitutive laws relevant for triggering a preexisting fault. Fault nucleation

DOI: 10.1002/nag

and criteria for propagating new faults are not included in this paper and will be addressed in the future work.

2.1. Rate- and state-dependent friction law

Laboratory tests on rough contacting surfaces sliding past each other strongly suggest the dependence of the coefficient of friction μ on rate of sliding as well as on a state variable reflecting the maturity of contact. For slow rate of sliding (on the order of microns per second), the constitutive law for μ that is currently in best agreement with experimental data is the Dieterich–Ruina friction law [30–32], expressed as

$$\mu = \mu^* + A \ln\left(\frac{V}{V^*}\right) + B \ln\left(\frac{\theta}{\theta^*}\right) \tag{1}$$

where V is the slip speed, θ is a state variable, and A, B, μ^*, V^*, and θ^* are material parameters. Two of these material parameters (typically V^* and θ^*) can be assigned arbitrary values since they only serve as normalizing constants. The state variable θ is linked to the changing set of frictional contacts and wear on the material, and evolves according to the equation

$$\dot{\theta} = 1 - \frac{\theta V}{D_c} \tag{2}$$

where D_c is a material parameter often referred to as the 'characteristic sliding distance' required to replace a contact population representative of a previous sliding condition with a contact population created under a new sliding condition [31]. For seismic faulting, D_c is the critical slip distance over which strength breaks down during earthquake nucleation [7]. Obviously, this characteristic distance scales with the problem analyzed (whether it be a meter-scale fracture or a kilometer-scale fault).

The physical significance of the constitutive law (1) is depicted in Figure 1. At a constant sliding velocity V_1, the coefficient of friction is μ_1. After a velocity time stepping to a higher velocity V_2, the coefficient of friction instantaneously increases by an amount $A \ln(V_2/V_1)$, and then decreases by an amount $B \ln(V_2/V_1)$ for a net decrease of $(A-B) \ln(V_2/V_1)$. Typically $B > A$, so a stepping to a faster speed results in net decrease in the coefficient of friction. The reverse is true for a stepping to a slower slip speed, i.e. the coefficient of friction instantaneously decreases first but

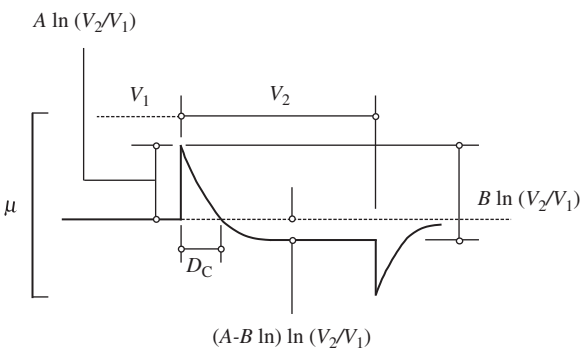

Figure 1. Variation of coefficient of friction μ in a velocity stepping test ($V_2 > V_1$).

DOI: 10.1002/nag

stabilizes to a higher value than the initial one prior to velocity stepping, for a net increase in the coefficient of friction. Also shown in Figure 1 is the characteristic slip D_c required to form a new contact population consistent with new velocity V_2.

Logarithmic functions generate a singularity when the argument is zero, and this is also true with constitutive law (1). However, by interpreting frictional resistance as a rate process, logarithmic functions can be regularized to accommodate zero slip speed. In this case, the constitutive law (1) can be rewritten as

$$\mu = A \sinh^{-1}\left[\frac{V}{2V^*}\exp\left(\frac{\mu^* + B\ln(\theta/\theta^*)}{A}\right)\right] \tag{3}$$

The above equation predicts $\mu = 0$ when $V = 0$, implying statistically, forward and backward jumps in a rate process cancel when there is no directional energy. Therefore, constitutive law (3) can be viewed as the complete Arrhenius equation with forward and backward jumps in a rate process, whereas Equation (1) can be considered as a truncated version of the Arrhenius equation considering forward jumps only [49–51]. By using the regularized form, the coefficient of friction can be quantified even in the regime of negligible slip speeds (such as in the neighborhood of an emerging fault).

2.2. *Slip weakening*

The concept of slip weakening leading to a rate- and state-dependent friction was motivated by the cohesive zone models for tensile fracture developed by Barenblatt [44], Dugdale [43], and Bilby *et al.* [45], and extended to the shear fracture problem by Ida [35] and Palmer and Rice [52]. To understand better this process we consider a rock through which a fracture is nucleating and propagating, as shown in Figure 2. At the rupture point we assume that fault slip ζ begins to accumulate, as defined by the integral

$$\zeta = \int_t \dot{\zeta}\,\mathrm{d}t \tag{4}$$

where the integration is taken over the slip path, see Figure 2(a).

Figure 2(b) shows the resolved nominal shear stress t_T decaying to a residual state value away from the tip of a propagating fault, where the cumulative slip ζ has exceeded a value $\zeta^* \approx 0.5$ mm for most rocks [39]. Figure 3 further depicts this narrow region of slip weakening [35], in which t_T decreases either linearly or nonlinearly with ζ (Figures 3(a) and (b), respectively). The shaded area G_{II} represents the shear fracture energy that has been correlated by many authors with the magnitude of an earthquake.

The slip-weakening law may be written in the linear form

$$\Phi = t_T - c + \mu t_N = 0 \tag{5}$$

where t_N and t_T are normal and shear components of traction on the fault plane, respectively, and c and μ are the cohesion and coefficient of friction on the same plane, respectively. With $\dot{\zeta} = V$ denoting the slip speed on the fault and $\dot{\zeta} = 0$ during fault nucleation, $\mu = 0$ initially and the initial shear resistance is therefore purely cohesive. As slip accumulates the coefficient of friction μ quickly increases according to the regularized friction law (3), while the cohesion c decays to zero. At the conclusion of slip weakening, the cohesion is zero and the shear resistance becomes purely frictional. The normal component t_N could vary during the slip-weakening process, and

DOI: 10.1002/nag

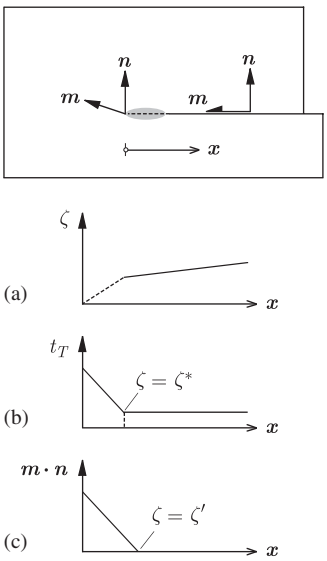

Figure 2. Model for fault nucleation and propagation in rock: (a) fault nucleates (dashed line) over a characteristic distance; (b) slip weakening takes place over characteristic slip ζ^*; and (c) initially dilatant volume change behavior on fault becomes isochoric over a characteristic slip ζ'. Figure reproduced from Borja [53].

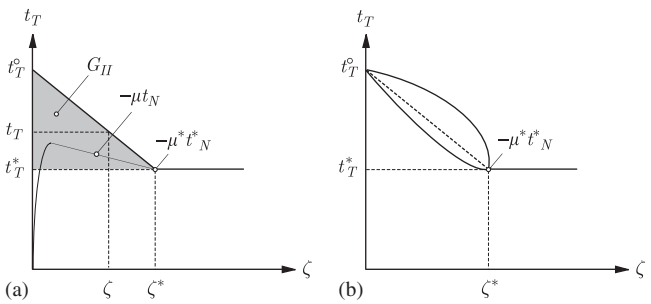

Figure 3. Slip-weakening models for rocks during fault nucleation: (a) linear slip weakening resulting from a combined cohesion softening–friction hardening on an emerging fault and (b) nonlinear slip weakening. Shaded area G_{II} represents shear fracture energy that has been correlated with the magnitude of an earthquake for seismic faulting, see Ida [35]. Figure reproduced from Borja [53].

since t_{T} depends on t_{N} through the coefficient of friction μ, a linear slip-weakening law such as the one depicted in Figure 3(a) is not trivially recovered from (5).

Borja and Foster [34] proposed a continuum mathematical model for slip weakening that is valid for any three-dimensional state of stress, including that characterizing a variable t_{N}. Assuming the shear resistance on the fault is purely frictional and the slip-weakening constitutive law is linear,

DOI: 10.1002/nag

an 'effective yield function' can be written in the form

$$\Phi = t_{\mathrm{T}} - \left[t_{\mathrm{T}}^{\circ} - (t_{\mathrm{T}}^{\circ} + \mu t_{\mathrm{N}}^{*}) \frac{\zeta}{\zeta^{*}} \right] \leqslant 0, \quad \zeta \in [0, \zeta^{*}] \tag{6}$$

where $\Phi = 0$ describes a linear slip weakening for a constant t_{N}. However, the condition $\Phi = 0$ is not a trivial linear constraint to impose since t_{N}^{*} is unknown during the slip-weakening process. A first-order approximation may be obtained by assuming $t_{\mathrm{N}}^{*} \approx t_{\mathrm{N}}$ [34], in which case (6) reduces to the form

$$\Phi = t_{\mathrm{T}} - \left[t_{\mathrm{T}}^{\circ} - (t_{\mathrm{T}}^{\circ} + \mu t_{\mathrm{N}}) \frac{\zeta}{\zeta^{*}} \right] \leqslant 0, \quad \zeta \in [0, \zeta^{*}] \tag{7}$$

This equation predicts a nonlinear slip weakening similar to Figure 3(b) for the case of a variable t_{N} (concave downwards or upwards depending on whether t_{N} decreases or increases during slip weakening), and recovers a linear slip weakening for the case of a constant t_{N}, see [21, 34] for further details.

2.3. Bulk plasticity

Damage surrounding a fault is produced by bulk plasticity. In particular, bulk plasticity in front of and surrounding a fault tip is responsible for fault extension and propagation. Bulk plasticity is not limited to the fault tip region, however. Depending on the relative yield strength of the host rock and the frictional resistance on the fault, plastic deformation can propagate outwards, causing the fault gouge to thicken as the fault continues to slide. Also, depending on loading condition, plastic deformation at distances much farther away from a preexisting fault can nucleate and rupture a new fault.

Computational plasticity has matured considerably over the last two decades (see the current advances in the book computational plasticity edited by Oñate and Owen [54]) that inclusion of bulk plasticity into the extended FE framework can now be done with relative ease, even for the case of frictional faulting [8, 15]. Obviously, the level of complexity of the solution depends very much on the plasticity model itself—highly elaborate yield functions and flow rules can contribute significantly to computational difficulty. In this paper we limit the plasticity model to (isotropic) functions of the first two stress invariants only. In general, these functions are sufficient to describe the constitutive responses of cohesive-frictional materials, including plastic dilatancy and compaction. Brittle faulting and cataclastic flow instabilities in rocks [53, 55] generally require a three-invariant constitutive formulation [56–58]. These more elaborate plasticity models will be considered in the future work so as not to digress too much from the focus of the present paper (i.e. frictional sliding).

3. FINITE ELEMENT EQUATIONS

This section focuses on the implementation of the variable friction law in the framework of the extended FE formulation. We recall briefly the definitions of problem domain and boundaries and refer the readers to [8, 15] for details of the variational formulation leading to the extended FE matrix equations.

DOI: 10.1002/nag

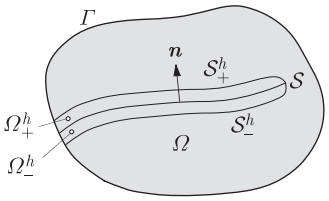

Figure 4. Definition of problem domain and boundaries. Domain Ω is cut by a fault $\mathscr{S}$. Compact support of $M_{\mathscr{S}}(\mathbf{x})$ is $\Omega^h = \Omega_-^h \cup \Omega_+^h$, and bounded by surfaces $\mathscr{S}_\pm^h$. Unit normal vector to $\mathscr{S}$ is $\mathbf{n}$, pointing in the direction of Ω_+^h. Fault tips may lie either on boundary Γ or inside domain Ω.

3.1. Problem definition

Consider a body Ω bounded by boundary Γ and cut by a fault $\mathscr{S}$ shown in Figure 4. Fault tips may lie either on the exterior boundary Γ or in the interior of Ω. The displacement field $\mathbf{u}$ is discontinuous on the fault according to the equation

$$\mathbf{u} = \overline{\mathbf{u}} + M_{\mathscr{S}}(\mathbf{x})\widetilde{\mathbf{u}} \tag{8}$$

where $\overline{\mathbf{u}}$ and $M_{\mathscr{S}}(\mathbf{x})\widetilde{\mathbf{u}}$ are the continuous and discontinuous parts of $\mathbf{u}$, respectively. The scalar function $M_{\mathscr{S}}(\mathbf{x})$ generates the discontinuity on the fault, and is given by the equation

$$M_{\mathscr{S}}(\mathbf{x}) = H_{\mathscr{S}}(\mathbf{x}) - f^h(\mathbf{x}) \tag{9}$$

where $H_{\mathscr{S}}(\mathbf{x})$ is a Heaviside function defined by

$$H_{\mathscr{S}}(\mathbf{x}) = \begin{cases} 1, & \mathbf{x} \in \Omega_+^h \\ 0, & \mathbf{x} \in \Omega_-^h \end{cases} \tag{10}$$

and $f^h(\mathbf{x})$ is any arbitrary smooth function that satisfies the requirements $f^h = 0$ on $\mathscr{S}_-^h$, and $f = 1$ on $\mathscr{S}_+^h$. The jump of $M_{\mathscr{S}}$ on $\mathscr{S}$ is $[\![M_{\mathscr{S}}]\!] = 1$, and $M_{\mathscr{S}} = 0$ on the surface $\mathscr{S}_\pm^h$ so that $\Omega^h = \Omega_+^h \cup \Omega_-^h$ serves as its compact support. Assuming infinitesimal deformation, the small strain tensor can be written as

$$\boldsymbol{\varepsilon} = \nabla^{\mathrm{s}}\mathbf{u} = \nabla^{\mathrm{s}}\overline{\mathbf{u}} + H_{\mathscr{S}}(\mathbf{x})\nabla^{\mathrm{s}}\widetilde{\mathbf{u}} - \nabla^{\mathrm{s}}(f^h(\mathbf{x})\widetilde{\mathbf{u}}) + \delta_{\mathscr{S}}(\widetilde{\mathbf{u}} \otimes \mathbf{n})^{\mathrm{s}} \tag{11}$$

where ∇^{s} is the symmetric spatial gradient operator, $(\cdot)^{\mathrm{s}}$ denotes the symmetric part of the tensor, $\delta_{\mathscr{S}}$ is the Dirac delta distribution function, and $\mathbf{n}$ is the unit normal vector to $\mathscr{S}$ and pointing toward Ω_+^h.

Without loss of generality we assume quasi-static loading and write the linear momentum balance equations as follows:

$$\operatorname{div}(\boldsymbol{\sigma}) + \mathbf{f} = \mathbf{0} \quad \text{in } \Omega \backslash \mathscr{S} \tag{12}$$

$$\mathbf{v} \cdot \boldsymbol{\sigma} = \mathbf{t} \quad \text{on } \Gamma_{\mathbf{t}} \tag{13}$$

where $\boldsymbol{\sigma}$ is the Cauchy stress tensor, $\mathbf{f}$ is the body force vector, $\mathbf{t}$ is the traction vector acting on external surface boundary $\Gamma_{\mathbf{t}}$, and $\mathbf{v}$ is the unit normal vector to $\Gamma_{\mathbf{t}}$. The above equations are

DOI: 10.1002/nag

augmented with the following conditions on the fault:

$$\mathbf{n}\cdot\boldsymbol{\sigma}=\mathbf{t}_{\mathscr{S}_-} \quad \text{on } \mathscr{S}_- \tag{14}$$

$$-\mathbf{n}\cdot\boldsymbol{\sigma}=\mathbf{t}_{\mathscr{S}_+} \quad \text{on } \mathscr{S}_+ \tag{15}$$

where $\mathscr{S}_-$ and $\mathscr{S}_+$ are sides of the fault taken to belong in Ω^h_- and Ω^h_+, respectively.

Outside Ω^h we assume a rate-independent elastoplastic constitutive relation between $\boldsymbol{\sigma}$ and $\boldsymbol{\varepsilon}$ of the form

$$\boldsymbol{\sigma}=\boldsymbol{\sigma}(\boldsymbol{\varepsilon}), \quad \mathbf{x}\in\Omega\backslash\Omega^h \tag{16}$$

Rate-dependent constitutive relations, such as elasto-viscoplasticity, can also be accommodated by the formulation although we shall limit this work to the rate-independent case. However, bulk deformation of any point in Ω^h is coupled with the relative displacement on the fault, so in this case the stress tensor $\boldsymbol{\sigma}$ could also depend on the strain rate tensor $\dot{\boldsymbol{\varepsilon}}$ through the velocity-dependent coefficient of friction, i.e.

$$\boldsymbol{\sigma}=\boldsymbol{\sigma}(\boldsymbol{\varepsilon},\dot{\boldsymbol{\varepsilon}}), \quad \mathbf{x}\in\Omega^h \tag{17}$$

Consider a 2D plane strain condition and write the gap function g_{N} and relative slip g_{T} on the fault as

$$g_{\mathrm{N}}(\mathbf{x},t)=\tilde{\mathbf{u}}(\mathbf{x},t)\cdot\mathbf{n}(\mathbf{x}), \quad g_{\mathrm{T}}(\mathbf{x},t)=\tilde{\mathbf{u}}(\mathbf{x},t)\cdot\mathbf{m}(\mathbf{x})\equiv\zeta(\mathbf{x},t) \tag{18}$$

where

$$\tilde{\mathbf{u}}(\mathbf{x},t)=\mathbf{u}_+(\mathbf{x},t)-\mathbf{u}_-(\mathbf{x},t) \tag{19}$$

is the relative displacement on the fault, $\mathbf{n}$ and $\mathbf{m}$ are unit normal and tangent vectors, and ζ is slip on the fault. We define normal and tangent components of the traction vector on the fault as

$$t_{\mathrm{N}}=\mathbf{t}_{\mathscr{S}_-}\cdot\mathbf{n}, \quad t_{\mathrm{T}}=\mathbf{t}_{\mathscr{S}_-}\cdot\mathbf{m} \tag{20}$$

Following the self-contact algorithm proposed in [8, 15], contact condition on the fault is imposed in the normal direction through the Kuhn–Tucker relations

$$g_{\mathrm{N}}\geqslant 0, \quad t_{\mathrm{N}}\leqslant 0, \quad g_{\mathrm{N}}t_{\mathrm{N}}=0 \tag{21}$$

The criteria for stick–slip may be cast in the framework of classical plasticity theory through the yield function $\Phi\leqslant 0$ of the form

$$\Phi=\begin{cases} t_{\mathrm{T}}-[t_{\mathrm{T}}^{\circ}-(t_{\mathrm{T}}^{\circ}+\mu t_{\mathrm{N}})\zeta/\zeta^*], & \zeta\in[0,\zeta^*] \\ t_{\mathrm{T}}+\mu t_{\mathrm{N}}, & \zeta\in[\zeta^*,\infty) \end{cases} \tag{22}$$

The above yield function encompasses the regimes of slip weakening (first line) and residual sliding (second line). Variable friction law is given by the regularized constitutive equation

$$\mu=A\sinh^{-1}\left[\frac{\dot{\zeta}}{2V^*}\exp\left(\frac{\mu^*+B\ln(\theta/\theta^*)}{A}\right)\right] \tag{23}$$

DOI: 10.1002/nag

along with the following evolution of the state variable θ:

$$\dot{\theta}=1-\frac{\theta\dot{\zeta}}{D_{\mathrm{c}}} \tag{24}$$

In principle, Equations (23) and (24) can be solved simultaneously to eliminate one variable, and for our purpose we shall eliminate the state variable θ and retain the coefficient of friction μ. Separate Kuhn–Tucker relations can be written to describe stick-slip conditions

$$\dot{\zeta}\geqslant 0, \quad \Phi\leqslant 0, \quad \dot{\zeta}\Phi=0 \tag{25}$$

3.2. Extended FE equations and time integration

The variational formulation for the model problem is presented in [8, 15] and will not be repeated here. Suffice it to say that the formulation consists of regular and enhancement parts capable of accommodating the propagation of frictional fault through the interior of FEs. The variational formulation differs from that of [11] in that frictional faulting is formulated in terms of the relative displacement $\widetilde{\mathbf{u}}$ on the fault, rather than the actual displacements $\mathbf{u}_+$ and $\mathbf{u}_-$ of each side of the fault, see (19). Thus, the formulation accommodates far more complex friction laws such as the one considered in this paper.

Let $\mathbf{d}$ denote the unknown regular nodal displacement vector and $\mathbf{a}$ the vector of nodal displacement enhancements. They define the continuous and discontinuous displacement fields through the interpolations

$$\overline{\mathbf{u}}=\mathbf{N}\mathbf{d}, \quad M_{\mathscr{S}}\widetilde{\mathbf{u}}=\widetilde{\mathbf{N}}\mathbf{a} \tag{26}$$

where $\mathbf{N}$ and $\widetilde{\mathbf{N}}$ are regular and enhanced shape function matrices, respectively (see [8, 15]). The vector $\mathbf{a}$ is used in the extended FE solution as global enrichments to accommodate displacement discontinuities, and is determined along with the regular displacement vector $\mathbf{d}$ in one simultaneous global equation solve. In the extended FE method two sets of FE equations must be solved simultaneously. The first is the equilibrium equation without a discontinuity,

$$\mathbf{F}_{\mathrm{INT}}(\mathbf{d},\dot{\mathbf{a}},\mathbf{a})=\mathbf{F}_{\mathrm{EXT}} \tag{27}$$

where

$$\mathbf{F}_{\mathrm{INT}}(\mathbf{d},\dot{\mathbf{a}},\mathbf{a})=\int_{\Omega\setminus\mathscr{S}}\mathbf{B}^{\mathrm{T}}\boldsymbol{\sigma}(\mathbf{d},\dot{\mathbf{a}},\mathbf{a})\,\mathrm{d}\Omega \tag{28}$$

$$\mathbf{F}_{\mathrm{EXT}}=\int_{\Omega}\mathbf{N}^{\mathrm{T}}\mathbf{f}\,\mathrm{d}\Omega+\int_{\Gamma}\mathbf{N}^{\mathrm{T}}\mathbf{t}\,\mathrm{d}\Omega \tag{29}$$

and $\mathbf{B}=\nabla^{\mathrm{s}}\mathbf{N}$. Dependence of $\boldsymbol{\sigma}$ on $\mathbf{a}$ and $\dot{\mathbf{a}}$ holds true only in the subdomain Ω^h.

The second set of FE equations pertains to the enhancements in Ω^h and takes the form

$$\mathscr{F}_{\mathrm{INT}}(\mathbf{d},\dot{\mathbf{a}},\mathbf{a})+\mathscr{G}_{\mathrm{INT}}(\dot{\mathbf{a}},\mathbf{a})=\mathscr{F}_{\mathrm{EXT}} \tag{30}$$

where

$$\mathscr{F}_{\mathrm{INT}}(\mathbf{d},\dot{\mathbf{a}},\mathbf{a})=\int_{\Omega^h\setminus\mathscr{S}}\widetilde{\mathbf{B}}^{\mathrm{T}}\boldsymbol{\sigma}(\mathbf{d},\dot{\mathbf{a}},\mathbf{a})\,\mathrm{d}\Omega \tag{31}$$

DOI: 10.1002/nag

$$\mathscr{G}_{\mathrm{INT}}(\dot{\mathbf{a}},\mathbf{a})=\int_{\mathscr{S}}\mathbf{N}^{\mathrm{T}}\mathbf{t}_{\mathscr{S}_-}(\dot{\mathbf{a}},\mathbf{a})\,\mathrm{d}\mathscr{S} \tag{32}$$

$$\mathscr{F}_{\mathrm{EXT}}=\int_{\Omega^h}\widetilde{\mathbf{N}}^{\mathrm{T}}\mathbf{f}\,\mathrm{d}\Omega+\int_{\Gamma^h}\widetilde{\mathbf{N}}^{\mathrm{T}}\mathbf{t}\,\mathrm{d}\Omega \tag{33}$$

and $\widetilde{\mathbf{B}}=\nabla^{\mathrm{s}}\widetilde{\mathbf{N}}$. The surface integral $\mathscr{G}_{\mathrm{INT}}$ arises from the displacement discontinuity on the fault and depends only on the vectors $\dot{\mathbf{a}}$ and $\mathbf{a}$, but not on $\mathbf{d}$. This surface integral accounts for the slip-weakening equation and variable friction law on the fault through the traction vector $\mathbf{t}_{\mathscr{S}_-}$. For a constant coefficient of friction, the FE equations do not depend on $\dot{\mathbf{a}}$.

We now assume that $\mathbf{d}_n$, $\dot{\mathbf{a}}_n$, and $\mathbf{a}_n$ are given converged nodal solution vectors from the previous time step. The problem is to find $\mathbf{d}_{n+1}$, $\dot{\mathbf{a}}_{n+1}$, and $\mathbf{a}_{n+1}$ such that

$$\mathbf{F}_{\mathrm{INT}}(\mathbf{d}_{n+1},\dot{\mathbf{a}}_{n+1},\mathbf{a}_{n+1})=(\mathbf{F}_{\mathrm{EXT}})_{n+1} \tag{34}$$

$$\mathscr{F}_{\mathrm{INT}}(\mathbf{d}_{n+1},\dot{\mathbf{a}}_{n+1},\mathbf{a}_{n+1})+\mathscr{G}_{\mathrm{INT}}(\dot{\mathbf{a}}_{n+1},\mathbf{a}_{n+1})=(\mathscr{F}_{\mathrm{EXT}})_{n+1} \tag{35}$$

This resembles a system of first-order ordinary differential equations that can be time-integrated using the generalized trapezoidal family of methods. Time integration is required only on the vector $\mathbf{a}$ and takes the form

$$\mathbf{a}_{n+1}=\mathbf{a}_n+[\beta\dot{\mathbf{a}}_{n+1}+(1-\beta)\dot{\mathbf{a}}_n]\Delta t \tag{36}$$

where Δt is the time increment and $\beta\in[0,1]$ is the time integration parameter (Crank–Nicolson if $\beta=\frac{1}{2}$, backward implicit if $\beta=1$, etc.). Equation (36) can be used to eliminate $\dot{\mathbf{a}}_{n+1}$, and thus express (34) and (35) in terms of $\mathbf{d}_{n+1}$ and $\mathbf{a}_{n+1}$ alone.

Introducing the operator $\widetilde{\mathbf{N}}$ on (36) and noting that the displacement jump on $\mathscr{S}$ is $[\![M_{\mathscr{S}}(\mathbf{x}_{\mathscr{S}})\widetilde{\mathbf{u}}(\mathbf{x}_{\mathscr{S}})]\!]=\widetilde{\mathbf{u}}(\mathbf{x}_{\mathscr{S}})$, we get

$$\widetilde{\mathbf{u}}_{n+1}=\widetilde{\mathbf{u}}_n+[\beta\dot{\widetilde{\mathbf{u}}}_{n+1}+(1-\beta)\dot{\widetilde{\mathbf{u}}}_n]\Delta t,\quad \mathbf{x}\in\mathscr{S} \tag{37}$$

Contracting with $\mathbf{m}$ and using the second of (18) gives the local time integration algorithm for slip,

$$\zeta_{n+1}=\zeta_n+[\beta\dot{\zeta}_{n+1}+(1-\beta)\dot{\zeta}_n]\Delta t \tag{38}$$

The above time-integrated form for slip permits a local time-marching scheme for the variable friction law.

To solve the coupled nonlinear problem we write (34) and (35) in residual form, dropping subscripts '$n+1$' for brevity

$$\mathbf{r}(\mathscr{D})=\begin{Bmatrix}\mathbf{F}_{\mathrm{EXT}}-\mathbf{F}_{\mathrm{INT}}\\ \mathscr{F}_{\mathrm{EXT}}-\mathscr{G}_{\mathrm{INT}}-\mathscr{F}_{\mathrm{INT}}\end{Bmatrix},\quad \mathscr{D}=\begin{Bmatrix}\mathbf{d}\\ \mathbf{a}\end{Bmatrix} \tag{39}$$

Newton's method can be used to solve this equation, which requires evaluating the consistent tangent operator

$$-\mathbf{r}'(\mathscr{D})=\begin{bmatrix}\mathbf{A}_{11} & \mathbf{A}_{12}\\ \mathbf{A}_{21} & \mathbf{A}_{22}\end{bmatrix} \tag{40}$$

DOI: 10.1002/nag

where

$$\mathbf{A}_{11}=\int_{\Omega}\mathbf{B}^{\mathrm{T}}\mathbf{D}\mathbf{B}\,\mathrm{d}\Omega,\quad \mathbf{A}_{12}=\int_{\Omega}\mathbf{B}^{\mathrm{T}}\mathbf{D}\widetilde{\mathbf{B}}\,\mathrm{d}\Omega$$
$$\mathbf{A}_{21}=\int_{\Omega^h}\widetilde{\mathbf{B}}^{\mathrm{T}}\mathbf{D}\mathbf{B}\,\mathrm{d}\Omega,\quad \mathbf{A}_{22}=\overline{\mathbf{A}}_{22}+\overline{\overline{\mathbf{A}}}_{22} \tag{41}$$
$$\overline{\mathbf{A}}_{22}=\int_{\Omega^h}\widetilde{\mathbf{B}}^{\mathrm{T}}\mathbf{D}\widetilde{\mathbf{B}}\,\mathrm{d}\Omega,\quad \overline{\overline{\mathbf{A}}}_{22}=\int_{\mathscr{S}}\mathbf{N}^{\mathrm{T}}\mathbf{E}\mathbf{N}\,\mathrm{d}\mathscr{S}$$

In the equations above, $\mathbf{D}$ is the algorithmic tangent operator of Simo and Taylor [59] for bulk plasticity, while

$$\mathbf{E}=\partial\mathbf{t}_{\mathscr{S}_-}/\partial\widetilde{\mathbf{u}} \tag{42}$$

is the algorithmic tangent operator for fault-plane plasticity. In general, both $\mathbf{D}$ and $\mathbf{E}$ are nonsymmetric matrices.

3.3. Local time integration for the variable friction law

Consider the regularized form of 'slowness' law imposed at time t_{n+1}:

$$\mu_{n+1}=A\sinh^{-1}\left[\frac{\dot{\zeta}_{n+1}}{2V^*}\exp\left(\frac{\mu^*+B\ln(\theta_{n+1}/\theta^*)}{A}\right)\right] \tag{43}$$

and

$$\dot{\theta}_{n+1}=1-\frac{\theta_{n+1}\dot{\zeta}_{n+1}}{D_{\mathrm{c}}} \tag{44}$$

For future use we shall also impose the state evolution Equation (44) at time t_n as

$$\dot{\theta}_n=1-\frac{\theta_n\dot{\zeta}_n}{D_{\mathrm{c}}} \tag{45}$$

Our objective is to eliminate one of the independent variables (i.e. θ_{n+1}) and express the coefficient of friction μ_{n+1} in terms of slip ζ_{n+1} alone.

Dropping subscript '$n+1$' once again for brevity, the time-integrated Equation (38) can be rewritten as

$$\dot{\zeta}=\frac{\zeta-\zeta_n}{\beta\Delta t}-\frac{1-\beta}{\beta}\dot{\zeta}_n,\quad \beta\neq 0 \tag{46}$$

In this equation we rule out the forward Euler scheme ($\beta=0$) since it does not possess desirable stability and accuracy properties anyway. Next, we multiply (44) by $\beta\Delta t$ and (45) by $(1-\beta)\Delta t$ and add the results to get

$$\theta-\theta_n=[\beta\dot{\theta}+(1-\beta)\dot{\theta}_n]\Delta t \tag{47}$$
$$=\Delta t\left[1-\frac{\beta}{D_{\mathrm{c}}}\theta\dot{\zeta}-\frac{1-\beta}{D_{\mathrm{c}}}\theta_n\dot{\zeta}_n\right] \tag{48}$$

DOI: 10.1002/nag

from which we get

$$\theta=\left(\theta_n+\Delta t-\frac{(1-\beta)\Delta t}{D_c}\theta_n\dot{\zeta}_n\right)\Big/\left(1+\frac{\Delta t\beta}{D_c}\dot{\zeta}\right) \tag{49}$$

Both $\dot{\zeta}$ and θ are now functions of ζ, so the coefficient of friction is now expressed in terms of slip ζ alone.

For future use, we also obtain the derivative $\mu'(\zeta)$ from successively applying the chain rule:

$$\mu'(\zeta)=\left(\frac{A}{\dot{\zeta}\beta\Delta t}-\frac{\alpha B}{(1+\alpha\dot{\zeta})\beta\Delta t}\right)\tanh\left(\frac{\mu}{A}\right),\quad \alpha=\frac{\Delta t\beta}{D_c} \tag{50}$$

3.4. Penalty method and derivatives

Without loss of generality, we shall assume a 2D plane strain representation of the prototype problem in what follows (see [8, 15] for the more general 3D formulation). Consider the following expression for the traction vector on the fault:

$$\mathbf{t}_{\mathscr{S}_-}=t_N\mathbf{n}+t_T\mathbf{m} \tag{51}$$

Thus, we obtain the tangent operator $\mathbf{E}$ as

$$\mathbf{E}=\mathbf{n}\otimes\frac{\partial t_N}{\partial\widetilde{\mathbf{u}}}+\mathbf{m}\otimes\frac{\partial t_T}{\partial\widetilde{\mathbf{u}}} \tag{52}$$

In [8, 15] it was shown that the penalty method can be used to enforce contact and slip conditions with sufficient accuracy in the context of the extended FE method. Contact condition (21) can be enforced in the approximate sense through a constitutive equation for the normal component of traction vector of the form

$$t_N=\varepsilon_N g_N \tag{53}$$

where $\varepsilon_N\gg 1$ is a penalty parameter analogous to a normal spring constant. Thus, from (18) we get

$$\frac{\partial t_N}{\partial\widetilde{\mathbf{u}}}=\varepsilon_N\mathbf{n} \tag{54}$$

Stick condition, $\dot{\zeta}=0$ and $\Phi<0$ in (25), can also be enforced in the approximate sense by a similar penalty approach. Consider the following rate constitutive law for the tangential component of traction:

$$\dot{t}_T=\varepsilon_T(\dot{g}_T-\dot{\zeta}) \tag{55}$$

where $\varepsilon_T\gg 1$ is a penalty parameter analogous to a tangential spring constant. Note that $\dot{g}_T$ can only equal $\dot{\zeta}$ in the limit as ε_T approaches infinity. The incremental version is easily derived as

$$t_T=(t_T)_n+\varepsilon_T(\Delta\widetilde{\mathbf{u}}\cdot\mathbf{m}-\Delta\zeta) \tag{56}$$

where $\Delta\widetilde{\mathbf{u}}=\widetilde{\mathbf{u}}-\widetilde{\mathbf{u}}_n$ and $\Delta\zeta=\zeta-\zeta_n$. Hence, for stick condition where $\Delta\zeta=0$ we get

$$\frac{\partial t_T}{\partial\widetilde{\mathbf{u}}}=\varepsilon_T\mathbf{m} \tag{57}$$

DOI: 10.1002/nag

On the other hand, for slip condition $\Delta\zeta \neq 0$, and so we get the derivative

$$\frac{\partial t_{\mathrm{T}}}{\partial \widetilde{\mathbf{u}}} = \varepsilon_{\mathrm{T}} \left(\mathbf{m} - \frac{\partial \zeta}{\partial \widetilde{\mathbf{u}}} \right) \tag{58}$$

The rest of the formulation boils down to the evaluation of the derivative $\partial\zeta/\partial\widetilde{\mathbf{u}}$ under a slip condition.

Slip condition, $\dot{\zeta}>0$ and $\Phi=0$ in (25), could activate one of two possible yield functions depending on whether the fault undergoes slip weakening or residual sliding. We consider these two cases separately below.

Case 1. Slip weakening: Assume $\zeta \in [0, \zeta^*]$. Substituting (56) into the slip-weakening law $(22)_1$ gives

$$r = (t_{\mathrm{T}})_n + \varepsilon_{\mathrm{T}}(\Delta\widetilde{\mathbf{u}}\cdot\mathbf{m} - \Delta\zeta) + t_{\mathrm{T}}^{\circ}\left(\frac{\zeta}{\zeta^*} - 1\right) + \varepsilon_{\mathrm{N}}\mu(\zeta)\frac{\zeta}{\zeta^*}\widetilde{\mathbf{u}}\cdot\mathbf{n} \tag{59}$$

We can imagine the scalar r as a residual function of ζ for a given $\widetilde{\mathbf{u}}$, i.e. $r=r(\zeta)$. We thus want to determine $\overline{\zeta}$ such that $r(\overline{\zeta})=0$. For a constant coefficient of friction this equation readily yields a closed-form solution for $\overline{\zeta}$. However, for the variable friction model this closed-form solution is not available, and an iterative scheme must be employed. Using Newton's method, we evaluate the Jacobian

$$\mathscr{A}(\zeta) = -r'(\zeta) = \varepsilon_{\mathrm{T}} - \frac{t_{\mathrm{T}}^{\circ}}{\zeta^*} - \varepsilon_{\mathrm{N}}\mu'(\zeta)\frac{\zeta}{\zeta^*}\widetilde{\mathbf{u}}\cdot\mathbf{n} - \varepsilon_{\mathrm{N}}\frac{\mu(\zeta)}{\zeta^*}\widetilde{\mathbf{u}}\cdot\mathbf{n} \neq 0 \tag{60}$$

where $\mu'(\zeta)$ is given by (50). The Newton iteration begins with an initial estimate $\zeta^0=\zeta_n$, and iterative updates are carried out of the form $\zeta^{k+1} \leftarrow \zeta^k + r(\zeta^k)/\mathscr{A}(\zeta^k)$. For future use we evaluate the derivative of r with respect to $\widetilde{\mathbf{u}}$ at the locally converged state $\overline{\zeta}$

$$\left.\frac{\partial r}{\partial \widetilde{\mathbf{u}}}\right|_{\overline{\zeta}} = \varepsilon_{\mathrm{T}}\mathbf{m} + \varepsilon_{\mathrm{N}}\mu(\overline{\zeta})\frac{\overline{\zeta}}{\zeta^*}\mathbf{n} \tag{61}$$

Case 2. Residual sliding: Assume $\zeta \in [\zeta^*, \infty)$. Substituting (56) into the residual yield function $(22)_2$ gives

$$r = (t_{\mathrm{T}})_n + \varepsilon_{\mathrm{T}}(\Delta\widetilde{\mathbf{u}}\cdot\mathbf{m} - \Delta\zeta) + \varepsilon_{\mathrm{N}}\mu(\zeta)\widetilde{\mathbf{u}}\cdot\mathbf{n} \tag{62}$$

Again, we want to determine slip $\overline{\zeta}$ such that $r(\overline{\zeta})=0$. Performing the same Newton iteration requires evaluating the Jacobian

$$\mathscr{A}(\zeta) = -r'(\zeta) = \varepsilon_{\mathrm{T}} - \varepsilon_{\mathrm{N}}\mu'(\zeta)\widetilde{\mathbf{u}}\cdot\mathbf{n} \neq 0 \tag{63}$$

and the same updates can be carried out as in Case 1. Furthermore, at the locally converged state, we have

$$\left.\frac{\partial r}{\partial \widetilde{\mathbf{u}}}\right|_{\overline{\zeta}} = \varepsilon_{\mathrm{T}}\mathbf{m} + \varepsilon_{\mathrm{N}}\mu(\overline{\zeta})\mathbf{n} \tag{64}$$

DOI: 10.1002/nag

Irrespective of whether the fault undergoes slip weakening or residual sliding, $r(\bar{\zeta}, \tilde{\mathbf{u}}) = 0$ at the locally converged state. Therefore, we can extract the derivative of this function with respect to $\tilde{\mathbf{u}}$ at the locally converged stress state as follows:

$$\frac{\partial r}{\partial \tilde{\mathbf{u}}} = \left.\frac{\partial r}{\partial \tilde{\mathbf{u}}}\right|_{\bar{\zeta}} + \frac{\partial r}{\partial \zeta}\frac{\partial \zeta}{\partial \tilde{\mathbf{u}}} = \mathbf{0} \tag{65}$$

We recall that $\partial r/\partial \zeta = -\mathscr{A}(\bar{\zeta})$ at the locally converged state. Hence,

$$\frac{\partial \zeta}{\partial \tilde{\mathbf{u}}} = [\mathscr{A}(\bar{\zeta})]^{-1} \left.\frac{\partial r}{\partial \tilde{\mathbf{u}}}\right|_{\bar{\zeta}} \tag{66}$$

Remark

That the contact and slip conditions are satisfied only in an approximate sense with the penalty method implies that slip ζ is no longer exactly equal to $\tilde{\mathbf{u}} \cdot \mathbf{m}$, see $(18)_2$. Hence, the local time-marching scheme for ζ with the generalized trapezoidal rule no longer corresponds to the same global time-marching scheme for the nodal enhancement vector $\mathbf{a}$, see, for example, the developments of Section 3.2. Nevertheless, this result is not critical since the extended FE formulation only involves the nodal values of displacements, $\mathbf{d}$ and $\mathbf{a}$, and not their rates.

4. NUMERICAL SIMULATIONS

We consider four examples in this section to demonstrate important features of the variable friction model and the performance of the algorithm. All examples pertain to plane strain condition with infinitesimal deformation.

4.1. Sliding of a pre-fractured granite block

This example consists of a $1\,\text{m} \times 1\,\text{m}$ granite block discretized into 18 constant strain triangular (CST) elements, with a horizontal discontinuity inserted in the middle of the mesh as shown in Figure 5. The upper block was sheared relative to the lower block, mimicking the experiment for granite with a #60 surface subjected to a 15 MPa normal stress [33]. The same experimental curve was earlier reproduced by Foster *et al*. [21] using the assumed enhanced strain FE formulation; here we used the same parameters along with the extended FE simulation. The slip speed began at $V_1 = 10^{-5}\,\text{m/s}$ for 2 s, increased to $V_2 = 10^{-4}\,\text{m/s}$ for 2 s, and finally decreased back to $V_3 = 10^{-5}\,\text{m/s}$ for 2 s. Time increment used in the simulation is $\Delta t = 0.002\,\text{s}$ and the total relative displacement is 0.24 mm after 6 s. The material properties used in the simulation are listed in Table I. The solution captures the variation in the coefficient of friction as shown in Figure 6. As slip speed is increased, we see the characteristic spike and subsequent drop to a lower steady-state value. Similarly, when the slip speed is decreased, the coefficient of friction dips and subsequently rises to a new, higher value. For comparison, we also computed the coefficient of friction directly from the numerical integration of the 'slowness' law presented in Section 3.3, and the results are shown in Table II. From Table II, we see that the calculated coefficients of friction are not significantly affected by the values of the penalty parameters. On a related note, Dieterich and Kilgore [33] showed that the coefficient of friction for the same material decreased by 10% when a 1 mm gouge was inserted between the crack.

DOI: 10.1002/nag

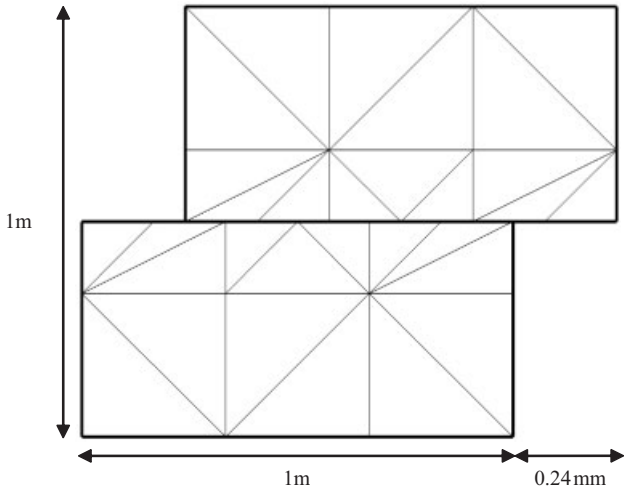

Figure 5. Deformed mesh for pre-fractured granite block (displacement magnified 1000 times). Horizontal failure surface passes halfway through the middle elements, which were divided into subtriangles for integration.

Table I. Mechanical properties for granite block shearing test.

Parameter	Symbol	Value
Young's modulus	E	5500 MPa
Poisson's ratio	ν	0.25
Friction parameter	μ^*	0.72
Friction parameter	A	0.012
Friction parameter	B	0.0135
Normalizing constant	V^*	1.0 μm/s
Normalizing constant	θ^*	2.25 s
Characteristic slip distance	D_c	2.25 μm
Slip-weakening distance	ζ^*	0.5 mm
Normal penalty parameter	ε_N	Varies
Tangential penalty parameter	ε_T	Varies

4.2. Plane strain compression of a fractured block

We next consider a rectangular block with a discontinuity oriented at 60° to the horizontal line shown in Figure 7. The FE mesh consists of 1024 CST elements and 561 nodes and was compressed vertically by prescribing a uniform downward displacement on top. The top and bottom boundaries were assumed smooth. The material parameters are listed in Table III. We assume that the continuum is an elastoplastic material yielding according to a nonassociated Drucker–Prager plasticity model, while the interface possessed initial cohesive strength, in addition to frictional strength developing with time, as defined by the Mohr–Coulomb failure criterion. In addition, a pressure of 250 MPa was applied on the vertical faces of the sample before applying the vertical compression so as to develop the full frictional strength of the interface.

DOI: 10.1002/nag

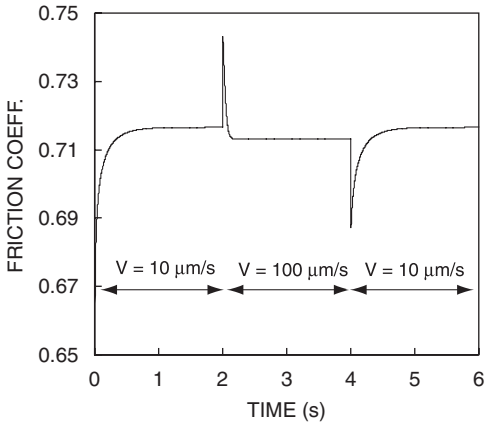

Figure 6. Coefficient of friction for granite block as a function of time under imposed sliding.

Table II. Calculated values of coefficient of friction μ. Numbers at $V = V_1$ and $V = V_2$ are steady-state values; pen = penalty parameter $= \varepsilon_N = \varepsilon_T$ [MN/m^3]; 'exact' = calculated from the time-integrated 'slowness' law.

Solution	Spike	Dip	$V = V_1$	$V = V_2$
Pen $= 10^6$	0.74311361	0.68699139	0.716544367	0.713092245
Pen $= 10^5$	0.74361349	0.68650022	0.716544427	0.713092245
Pen $= 10^4$	0.74361366	0.68649745	0.716544427	0.713092245
'Exact'	0.74314506	0.68649138	0.716544379	0.713092245

The results of the simulation are shown in Figure 8. The specimen behaves elastically in the beginning, then begins to yield when the vertical compression reaches around 0.5 mm. At a vertical displacement of around 0.8 mm the initial strength of the crack is reached, triggering a slip-weakening mechanism in which the initial cohesion of the interface decreases to zero as the full frictional strength picks up over a characteristic distance of $\zeta^* = 0.5$ mm. To demonstrate the properties of the state variable friction model at post-failure, we added a velocity jump to the simulation. The initial rate of vertical compression is 0.866 μm/s, which is equivalent to a slip speed of $\dot{\zeta} = 1.0\,\mu$m/s at steady state. The initial coefficient of friction is thus equal to μ^* from Table III. The rate of compression was then increased 10 times, resulting in an initial jump up and subsequent decrease of the coefficient of friction at steady state.

Contours of vertical displacement and bulk plastic strain at the conclusion of the simulation (when the vertical compression was around 3 mm) are shown in Figure 9. Note that plastic deformation is quite pronounced near the interface. This suggests that where the strength of the interface is comparable to the yield strength of the continuum, the crack thickness could potentially grow. The mechanism is similar to the thickening of a fault gouge, which can be more closely simulated by performing a bifurcation analysis on the yielded zone adjacent to the existing crack. We did not perform such a bifurcation analysis in this example.

DOI: 10.1002/nag

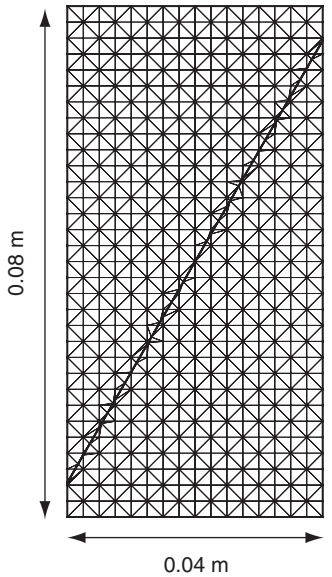

Figure 7. FE mesh for a rectangular block with a 60° frictional crack subjected to vertical compression.

Table III. Mechanical properties of rectangular fractured block subjected to vertical compression.

Parameter	Symbol	Value
Young's modulus	E	90 000 MPa
Poisson's ratio	v	0.15
Drucker-Prager cohesion parameter	$\overline{A}$	8.0 MPa
Drucker-Prager friction parameter	$\overline{B}$	0.633
Drucker-Prager dilatancy parameter	b	0.633
Initial interface cohesion	c_0	30 MPa
Interface friction parameter	μ^*	0.72
Interface friction parameter	A	0.012
Interface friction parameter	B	0.0135
Normalizing constant	V^*	1.0 μm/s
Normalizing constant	θ^*	2.25 s
Characteristic slip distance	D_c	2.25 μm
Slip-weakening distance	ζ^*	0.5 mm
Normal penalty parameter	ε_N	10^6 MN/m^3
Tangential penalty parameter	ε_T	10^6 MN/m^3

4.3. Square elastoplastic block with an internal crack

The FE mesh consists of 5000 cross-diagonal CST elements defined by 2601 nodes shown in Figure 10. The domain has in-plane dimensions of 1 m × 1 m (square) and contains a crack 0.566 m long oriented at 45° relative to the horizontal. In order for the crack to not intersect the nodes, the tips were specified at coordinates (0.29999,0.29998) and (0.70002,0.70001) m. Again, the standard

DOI: 10.1002/nag

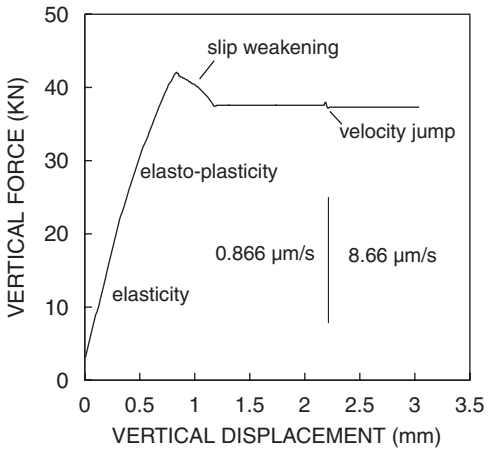

Figure 8. Vertical force versus vertical displacement for plane strain vertical compression of a fractured block showing different stages of deformation.

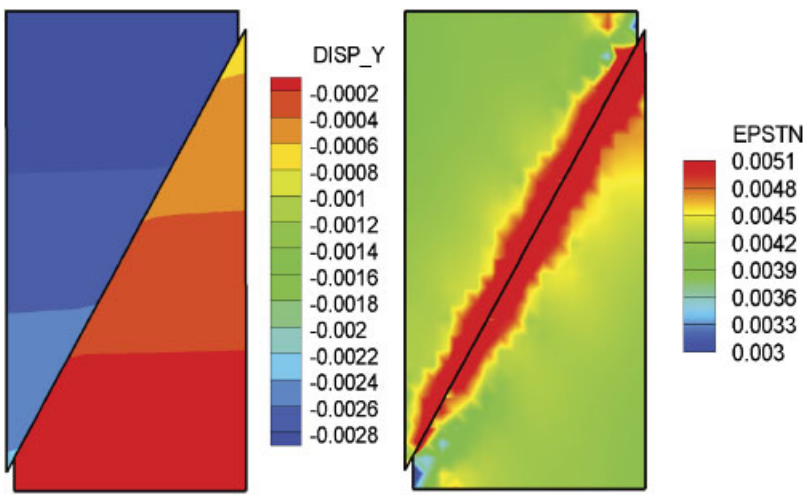

Figure 9. Contours of vertical displacement (left) and cumulative plastic strain (right). Plastic strain concentrates near the crack faces, suggesting potential for thickening of the fracture zone.

procedure of introducing more Gauss points in the vicinity of the crack was employed. The material parameters are the same as those listed in Table III except that we used bulk plasticity parameters $\overline{A} = 8.0\,\text{MPa}$ and $\overline{B} = b = 1.0$. The body was deformed by applying a uniform vertical compression at the top while allowing the top and the bottom nodes to move horizontally (smooth boundaries). We assumed that the crack could slide but the crack tip may not advance. The rate of vertical compression was prescribed at $10\,\mu\text{m/s}$ until a final vertical compression of 3 mm was reached.

Figure 11 shows the contour of vertical displacement at the last time step. Figure 12 suggests that bulk plasticity is localized around the crack tips, a similar result to that reported by Liu and

DOI: 10.1002/nag

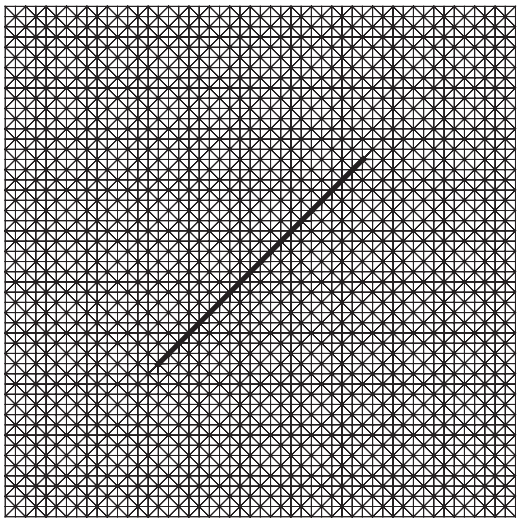

Figure 10. Finite element mesh for square elastoplastic block with an internal crack. The mesh is 1 m × 1 m with a frictional crack 0.566 m long oriented at 45° relative to the horizontal.

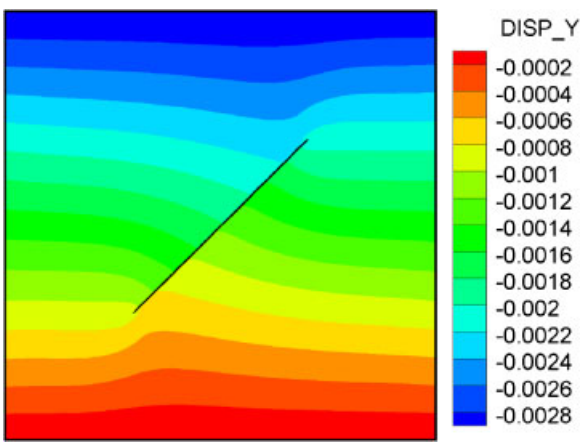

Figure 11. Contour of vertical displacement on deformed elastoplastic solid with an internal frictional crack. Displacement bar in meters.

Borja [15] for a crack with a constant coefficient of friction. Figure 13 portrays the effect of slip weakening on the load–displacement responses. Note that the vertical force versus vertical displacement curve at a compression rate of 10 μm/s is closer to the curve corresponding to a constant cohesion $c = 30$ MPa before weakening, and to a constant cohesion $c = 0$ MPa curve after weakening. To demonstrate the effect of the loading rate on the vertical force versus vertical displacement responses, we considered the loading rate of 1.0 μm/s for reference and plot the differences in responses for various rates of loading in Figure 14. Since the coefficient of friction

DOI: 10.1002/nag

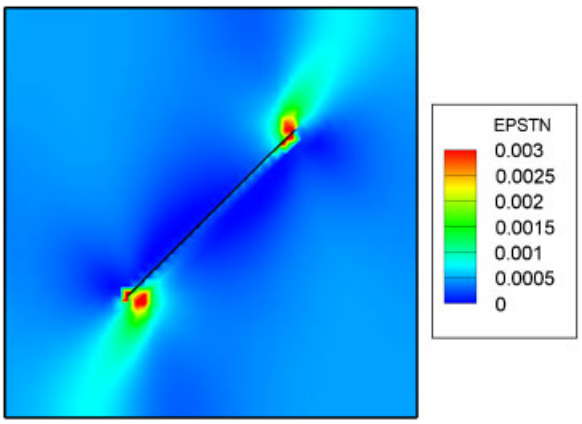

Figure 12. Contour of cumulative deviatoric plastic strain on deformed elastoplastic solid with an internal frictional crack at a vertical compression of 3 mm.

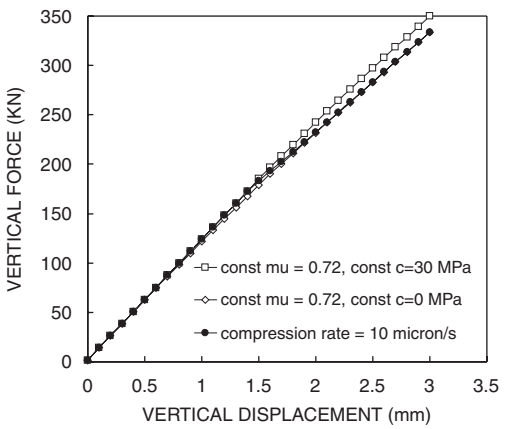

Figure 13. Vertical force versus vertical displacement for elastoplastic solid with an internal frictional crack.

decreases with slip speed, the vertical force reaction also decreases as the rate of loading increases, and this is reflected as negative differences in Figure 14. Finally, Figure 15 shows the convergence profile of Newton iterations clearly demonstrating the efficacy and efficiency of the iterative technique.

4.4. Curved crack under compressive loading

The final example is a 'miniature' version of the kilometer-scale model presented by Sanz *et al*. [46] for faulting and folding processes in geological structure. In the present example we considered a $1\,\mathrm{m} \times 0.5\,\mathrm{m}$ rectangular block with a curved frictional crack defined by 4900 CST elements and 2556 nodes shown in Figure 16. The elastoplastic block material has the same properties as those used in Example 3. A total horizontal compression of 3 mm was applied at the rate of $10\,\mu\mathrm{m/s}$,

DOI: 10.1002/nag

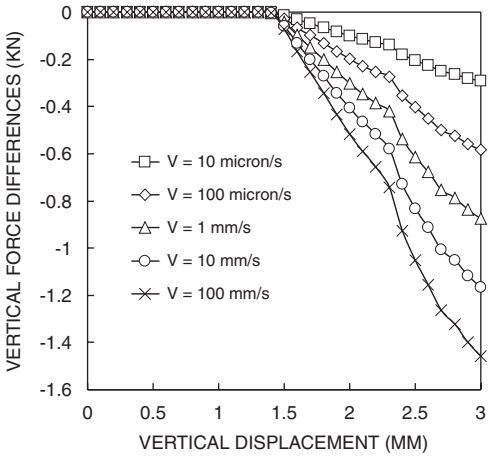

Figure 14. Effect of loading rate on the vertical force versus vertical displacement responses of the elastoplastic solid with an internal frictional crack.

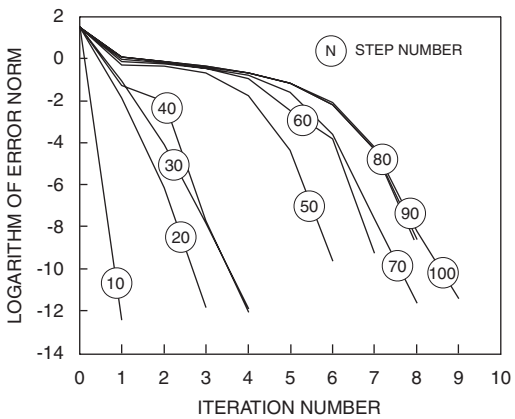

Figure 15. Convergence profile of Newton iterations for elastoplastic solid with an internal frictional crack. Error pertains to L_2-norm of residual force vector. All time steps converged to machine precision in less than 10 iterations.

assuming the vertical sides to be smooth. Because of the imposed uniform horizontal compression, there was no relative slip on the crack near the left vertical face. Furthermore, since the crack is curved the slip rate varied spatially throughout the fracture zone. It thus follows that the post-failure yield criterion also varied spatially throughout the crack, with some portion of the crack undergoing residual sliding while the rest were still undergoing slip weakening. Figure 17 shows the contour of cumulative plastic strain indicating that bulk plasticity concentrated around the crack tip. Some minor plastic deformation also was observed in the region of maximum curvature where the crack transitioned from horizontal to inclined positions.

DOI: 10.1002/nag

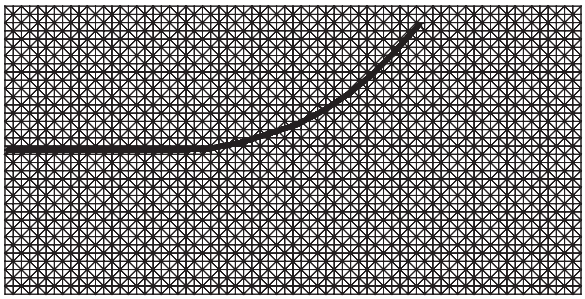

Figure 16. Finite element mesh for rectangular block with a curved frictional crack.

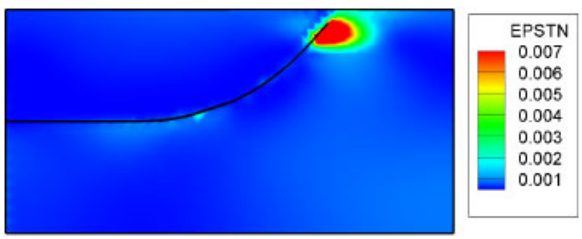

Figure 17. Cumulative deviatoric plastic strain for rectangular block with a curved frictional crack after a horizontal compression of 3 mm.

5. SUMMARY AND CONCLUSIONS

We have presented an extended FE framework for frictional faulting considering the combined effects of bulk plasticity and variable friction in a 2D plane strain setting. Under the assumption of infinitesimal deformation, we have implemented a regularized velocity- and state-dependent friction law that is currently in best agreement with experimental data for a variety of rocks, glass, acrylic plastic, and other frictional materials with bare surfaces at contact and rubbing against each other. The goal of the work was to formulate a robust framework that can eventually be used for modeling faulting in geological media. Bulk plasticity has been included in the formulation since it could potentially trigger fault rupture and extension as plastic yielding concentrates around the fault tip. However, numerical examples have also demonstrated that bulk plasticity could be responsible for increasing the thickness of the fault gouge in situations where the frictional strength of the fault is comparable to the yield strength of the host rock.

The Dieterich–Ruina friction law implemented in this work is valid for slow rate of sliding (on the order of microns per second), whereas actual seismic faulting could involve slip speeds that are several orders of magnitude faster. Geophysical insight into seismic faulting strongly suggests that the actual values of coefficient of friction could be much smaller than those measured in the laboratory [1, 60–62]. Furthermore, earthquake fault mechanisms could involve flash heating, fluid flow, and other highly complicated mechanisms not covered in the proposed framework. Nevertheless, the extended FE framework proposed in this paper shows great promise in handling some if not most of these complex mechanisms. This is demonstrated by the fact that the ‘slowness’ friction law considered in this paper involves exponential terms that are complex enough to

DOI: 10.1002/nag

challenge any robust nonlinear equation solver, yet the Newton iteration advocated in this work still delivered optimal performance. We thus believe that the proposed framework can be readily extended to accommodate other more complex faulting mechanisms not considered in this work.

ACKNOWLEDGEMENTS

This work is supported by the US Department of Energy Grant No. DE-FG02-03ER15454, and National Science Foundation Grant No. CMG-0417521 (Collaborations in Mathematical Geosciences). The first author acknowledges a Stanford Graduate Fellowship support.

REFERENCES

1. Scholz CH. *The Mechanics of Earthquakes and Faulting*. Cambridge University Press: New York, 1990.
2. Scholz CH. Earthquake and friction laws. *Nature* 1998; **391**:37–42.
3. Aydin A, Borja RI, Eichhubl P. Geological and mathematical framework for failure modes in granular rock. *Journal of Structural Geology* 2006; **28**:83–98.
4. Byerlee JD. Theory of friction based on brittle fracture. *Journal of Applied Physics* 1967; **38**:2928–2934.
5. Cooke ML. Fracture localization along faults with spatially varying friction. *Journal of Geophysical Research* 1997; **102**:22425–22434.
6. Marone C, Raleigh CB, Scholz CH. Frictional behavior and constitutive modeling of simulated fault gouge. *Journal of Geophysical Research* 1990; **95**:7007–7025.
7. Marone C, Kilgore B. Scaling of the critical slip distance for seismic faulting with shear strain in fault zones. *Nature* 1993; **362**:618–621.
8. Borja RI. Assumed enhanced strain and the extended finite element methods: a unification of concepts. *Computer Methods in Applied Mechanics and Engineering* 2008; **197**:2789–2803.
9. Belytschko T, Black T. Elastic crack growth in finite elements with minimal remeshing. *International Journal for Numerical Methods in Engineering* 1999; **45**:601–620.
10. Chessa Z, Wang H, Belytschko T. On the construction of blending elements for local partition of unity enriched finite elements. *International Journal for Numerical Methods in Engineering* 2003; **57**:1015–1038.
11. Dolbow J, Moes N, Belytschko T. An extended finite element method for modeling crack growth with frictional contact. *Computer Methods in Applied Mechanics and Engineering* 2001; **190**:6825–6846.
12. Elguedj T, Gravouil A, Combescure A. A mixed augmented Lagrangian-extended finite element method for modeling elastic–plastic fatigue crack growth with unilateral contact. *International Journal for Numerical Methods in Engineering* 2007; **71**:1569–1597.
13. Khoei AR, Shamloo A, Azami AR. Extended finite element method in plasticiy forming of powder compaction with contact friction. *International Journal of Solids and Structures* 2006; **43**:5421–5448.
14. Kim TY, Dolbow J, Laursen T. A mortared finite element method for frictional contact on arbitrary interfaces. *Computational Mechanics* 2007; **39**:223–235.
15. Liu F, Borja RI. A contact algorithm for frictional crack propagation with the extended finite element method. *International Journal for Numerical Methods in Engineering* 2008; **76**:1489–1512. DOI: 10.1002/nme.2376.
16. Sukumar N, Prevost JH. Modeling quasi-static crack growth with the extended finite element method Part I: computer implementation. *International Journal of Solids and Structures* 2003; **40**:7513–7537.
17. Wells GN, Sluys LJ. Three-dimensional embedded discontinuity model for brittle fracture. *International Journal of Solids and Structures* 2001; **38**:897–913.
18. Armero F, Garikipati K. Recent advances in the analysis and numerical simulation of strain localization in inelastic solids. In *Proceedings of Computational Plasticity IV*, Owen DRJ, Onate E, Hinton E (eds). CIMNE: Barcelona, Spain, 1995; 547–561.
19. Borja RI. A finite element model for strain localization analysis of strongly discontinuous fields based on standard Galerkin approximations. *Computer Methods in Applied Mechanics and Engineering* 2000; **190**:1529–1549.
20. Borja RI, Regueiro RA. Strain localization in frictional materials exhibiting displacement jumps. *Computer Methods in Applied Mechanics and Engineering* 2001; **190**:2555–2580.
21. Foster CD, Borja RI, Regueiro RA. Embedded strong discontinuity finite elements for fractured geomaterials with variable friction. *International Journal for Numerical Methods in Engineering* 2007; **72**:549–581.

22. Jirásek M. Comparative study on finite elements with embedded discontinuities. *Computer Methods in Applied Mechanics and Engineering* 2000; **188**:307–330.
23. Larsson R, Runesson K, Sture S. Embedded localization band in undrained soil based on regularized strong discontinuity theory and FE analysis. *International Journal of Solids and Structures* 1996; **33**:3081–3101.
24. Oliver J, Huespe AE. Theoretical and computational issues in modeling material failure in strong discontinuity scenarios. *Computer Methods in Applied Mechanics and Engineering* 2004; **193**:2987–3014.
25. Simo JC, Rifai MS. A class of mixed assumed strain methods and the method of incompatible modes. *International Journal for Numerical Methods in Engineering* 1990; **29**:1595–1638.
26. Simo JC, Oliver J, Armero F. An analysis of strong discontinuities induced by strain-softening in rate-independent inelastic solids. *Computational Mechanics* 1993; **12**:277–296.
27. Simo JC, Oliver J. A new approach to the analysis and simulation of strain softening in solids. In *Fracture and Damage in Quasibrittle Structures*, Bazant ZP, Bittnar Z, Jirásek M, Mazars J (eds). E&FN Spon: London, 1994.
28. Chester FM, Evans JP, Beigel RL. Internal structure and weakening mechanisms of the San Andreas fault. *Journal of Geophysical Research* 1993; **98**:771–786.
29. Beeler NM, Tulis TE, Weeks JD. The roles of time and displacement in the evolution effect in rock friction. *Geophysical Research Letters* 1994; **21**:1987–1990.
30. Dieterich JH. Time dependent friction and the mechanics of stick slip. *Pure and Applied Geophysics* 1978; **116**:790–806.
31. Dieterich JH. Modeling of rock friction 1. Experimental results and constitutive equations. *Journal of Geophysical Research* 1979; **84**:2161–2168.
32. Ruina AL. Slip instability and state variable friction laws. *Journal of Geophysical Research* 1983; **88**:10359–10370.
33. Dieterich JH, Kilgore BD. Direct observation of frictional contacts: new insights for state-dependent properties. *Pure and Applied Geophysics* 1994; **143**:283–302.
34. Borja RI, Foster CD. Continuum mathematical modeling of slip weakening in geological systems. *Journal of Geophysical Research* 2007; **112**(B04301). DOI: 10.1029/2005JB004056.
35. Ida Y. Cohesive force across the tip of a longitudinal shear crack and Griffith's specific surface energy. *Journal of Geophysical Research* 1972; **77**:3796–3805.
36. Okubo PG, Dieterich JH. Effects of physical fault properties on frictional instabilities produced on simulated faults. *Journal of Geophysical Research* 1984; **89**:5817–5827.
37. Rice JR. The mechanics and earthquake rupture. In *Physics of the Earth's Interior*, Dziewonski AM, Boschi E (eds). Elsevier: NY, 1980; 555–649.
38. Rummel F, Alheid HJ, Frohn C. Dilatancy and fracture-induced velocity changes in rock and their relation to frictional sliding. *Pure and Applied Geophysics* 1978; **116**:743–764.
39. Wong T. Shear fracture energy of westerly granite from post-failure behavior. *Journal of Geophysical Research* 1982; **87**:990–1000.
40. Wong T. On the normal stress dependence of the shear fracture energy. In *Earthquake Source Mechanics*, *Geophysical Monograph Series*, Das S, Boatwright J, Scholz CH (eds), vol. 37. AGU: Washington DC, 1986; 1–11.
41. Irwin GR. In *Fracture*, *Handbuck der Physik VI*, Flügge S (ed.). Springer: Berlin, 1958; 551–590.
42. Irwin GR. Plastic zone near a crack and fracture toughness. *Proceedings of the 7th Sagamore Conference*, Racquette Lake, New York, 1960; IV–63.
43. Dugdale DS. Yielding of steel sheets containing slits. *Journal of the Mechanics and Physics of Solids* 1960; **8**:100–108.
44. Barenblatt GI. The mathematical theory of equilibrium of cracks in brittle fracture. *Advances in Applied Mechanics* 1962; **7**:55–129.
45. Bilby BA, Cottrell AH, Swindon KH. The spread of plastic yield from a notch. *Proceedings of the Royal Society of London Series* 1963; **A272**:304–314.
46. Sanz PF, Borja RI, Pollard DD. Mechanical aspects of thrust faulting driven by far-field compression and their implications for fault geometry. *Acta Geotechnica* 2007; **2**:17–31.
47. Sanz PF, Pollard DD, Allwardt PF, Borja RI. Mechanical models of fracture reactivation and slip on bedding surfaces during folding of the asymmetric anticline at Sheep Mountain, Wyoming. *Journal of Structural Geology* 2008; **30**(9):1177–1191. DOI: 10.1016/j.jsg.2008.06.002.
48. Crisfield MA. *Non-linear Finite Element Analysis of Solids and Structures*, vol. 2. Wiley: New York, 1997.
49. Chester FM, Higgs NG. Multi-mechanism frictions constitutive model for ultra-fine quartz gouge at hypocentral conditions. *Journal of Geophysical Research* 1992; **97**:1859–1870.

50. Lapusta N, Rice JR, Ben-Zion Y, Zheng G. Elastodynamic analysis for slow tectonic loading with spontaneous rupture episodes on faults with rate- and state-dependent friction. *Journal of Geophysical Research* 2000; **105**:23765–23789.
51. Rice JR, Cocco M. Seismic fault rheology and earthquake dynamics. In *Tectonic Faults*: *Agents of Change on a Dynamic Earth*, Handy MR, Hirth G, Hovius N (eds). *Dahlem Workshop 95*. The MIT Press: Cambridge, MA, 2007; 99–137.
52. Palmer AC, Rice JR. The growth of slip surfaces in the progressive failure of overconsolidated clay. *Proceedings of the Royal Society of London Series* 1973; **332**:527–548.
53. Borja RI. Localized and diffuse bifurcations in porous rocks undergoing shear localization and cataclastic flow. In *Computational Plasticity* (*Computational Methods in Applied Sciences*), Oñate E, Owen R (eds). Springer: Berlin, 2007.
54. Onate E, Owen R. *Computational Plasticity*. Springer: Berlin, Heidelberg, 2007; 268.
55. Paterson MS, Wong T. *Experimental Rock Deformation—The Brittle Field*. Springer: Berlin, Heidelberg, 2005; 347.
56. Borja RI, Sama KM, Sanz PF. On the numerical integration of three-invariant elastoplastic constitutive models. *Computer Methods in Applied Mechanics and Engineering* 2003; **192**:1227–1258.
57. Borja RI, Aydin A. Computational modeling of deformation bands in granular media. I. Geological and mathematical framework. *Computer Methods in Applied Mechanics and Engineering* 2004; **193**:2667–2698.
58. Borja RI. Computational modeling of deformation bands in granular media. II. Numerical simulations. *Computer Methods in Applied Mechanics and Engineering* 2004; **193**:2699–2718.
59. Simo JC, Taylor RL. Consistent tangent operator for rate-independent elastoplasticity. *Computer Methods in Applied Mechanics and Engineering* 1985; **48**:101–118.
60. Cohen P. Inside the San Andreas. *New Scientist* 1997; **149**:24–27.
61. Di Toro G, Goldsby DL, Tullis TE. Friction falls toward zero in quartz rock as slip velocity approaches seismic rates. *Nature* 2004; **427**:436–439.
62. Marone C. Faults greased at high speed. *Nature* 2004; **427**:405–406.

DOI: 10.1002/nag